


Corrections on formation energies and eigenvalues of point defect calculations in two-dimensional materials

Yu Kumagai ^{*}*Institute for Materials Research, Tohoku University, 2-1-1 Katahira, Aoba-ku, Sendai 980-8577, Japan*

(Received 28 November 2023; revised 16 January 2024; accepted 30 January 2024; published 14 February 2024)

When applying two-dimensional materials in advanced electronics, catalysts, and quantum computing, point defects play crucial roles. However, experimentally determining the local structures and charge states of these defects is challenging, and the use of first-principles calculations is beneficial. Yet the number of studies in this area remains limited compared to those on three-dimensional materials, which is primarily due to difficulties in corrections related to finite model sizes. In this study, we introduce a method to automate these corrections and to reduce computational costs. Furthermore, we explore the impact of ill-defined dielectric profiles on the corrections and demonstrate that the selection of the profiles potentially affects the corrections for defects far from the surfaces significantly. We also illustrate how to correct the eigenvalues of host-derived orbitals in calculations of charged defects.

DOI: [10.1103/PhysRevB.109.054106](https://doi.org/10.1103/PhysRevB.109.054106)

I. INTRODUCTION

Two-dimensional (2D) semiconductors have attracted considerable attention in recent years due to their promise in advanced electronics [1], catalysis [2], energy storage [3], sensing [4], and quantum computing [5]. Point defects are pivotal in determining the electrical, ionic, and photocatalytic properties of 2D materials [1], making their control essential for optimizing performance. In contrast to their three-dimensional (3D) counterparts, defects in 2D materials can be directly observed using techniques like scanning tunneling microscopy [6]. However, routinely employing these experimental methods is challenging due to the requirements for sample preparation and specialized measurement skills. Moreover, experimentally determining the transition levels and defect charge states remains a daunting task.

First-principles calculations are increasingly used to study dominant point defects in 2D materials [7–17]. However, the number of studies on these defects is still limited compared to those on 3D materials. A major reason for this limitation is the difficulty in finite size corrections, which are crucial for calculating charged defects under periodic boundary conditions (PBCs). Several groups have reported methods to correct defect formation energies, yet routinely applying these techniques in practical applications remains challenging [7–15]. This is because each defect charge combination requires a unique correction process. Considering typical native defects in 2D materials, such as vacancies, antisites, interstitials, and adsorbed atoms, requires calculations of dozens of defect charge combinations. Therefore, automating the correction process and minimizing computational costs is vital for advancing defect calculations in 2D materials. To this end, we

introduce an interpolation technique to lessen computational costs and simplify the processes.

The functional forms of the dielectric profiles have been used as inputs for most correction methods proposed to date [7–12]. Unfortunately, these profiles are, in principle, ill defined, as will be discussed later. Although the dielectric profiles were previously thought to minimally impact the correction energies [8,11], we will explore the extent of this influence on energy corrections using various types of defects. Consequently, we find the correction energies for defects with charge centers far from surfaces can be significantly affected by the choice of dielectric profiles.

To effectively understand defect properties, it is crucial to distinguish defect-induced eigenvalues from those of host-derived bands. While the need for finite cell size corrections for eigenvalues of localized defect states has been recognized [7], discussions regarding host-derived bands are lacking. Unlike in 3D systems, the eigenvalues of host-derived bands in 2D systems deviate significantly from those of pristine bulk states. This deviation is due to the spurious electrostatic potential caused by the defect and background charge. To correct these artificial shifts, we propose aligning the electrostatic potential in the region where the 2D material exists. We evaluate its effectiveness and that of previously suggested corrections for the defect-induced eigenvalues.

Overall, our study primarily focuses on three key areas: First, we introduce a simpler and faster correction method for defect formation energies and defect-induced eigenvalues, utilizing the interpolation technique. Second, we assess the potential errors arising from the uncertainty in the dielectric profile. Third, we propose a method to correct the eigenvalues of host bands in the charged defect calculations. This paper is organized as follows: In Sec. II, we introduce the correction method developed by Noh *et al.* [14] and Komsa *et al.* [11] and the formula for calculating the isolated Gaussian charge developed by Sundararaman and Ping [21]. In Sec. III, we present

^{*}yukumagai@tohoku.ac.jp

the details of the first-principles calculations. In Sec. IV, we discuss the automation of the corrections for defect formation energies in detail. Here, we propose interpolating the long-range electrostatic interaction energies as a function of the defect charge position and evaluating alignment terms via one-dimensional (1D) electrostatic potentials. In Sec. V, we investigate the influence of dielectric profiles using defects in single-layer (SL) MoS₂ and SL hexagonal BN (h-BN) as examples. We also discuss how to correct the eigenvalues of host-derived states and demonstrate the accuracy of these corrections. Finally, we summarize the paper in Sec. VI.

II. CORRECTION METHOD FOR DEFECT FORMATION ENERGIES

In this study, we employ the correction method proposed by Noh *et al.* [14] and Komsa *et al.* [11] (NK method), which extends the Freysoldt–Neugebauer–Van de Walle (FNV) method [18] to 2D systems. For simplicity, we focus on tetragonal systems and align the directions perpendicular to the surfaces with the z direction.

Assuming that the defect charge is enclosed in the supercell, the correction energy at defect charge q can be expressed as [11,14]

$$E_{\text{corr}}^{\sigma} = \Delta E_{\text{lr}}^{\sigma,q}(z_0) + q\bar{V}_{\text{corr}}^{\sigma,q}(z_0, z_{\text{far}}), \quad (1)$$

where $\Delta E_{\text{lr}}^{\sigma,q}$ is the correction energy for long-range (lr) electrostatic interaction, defined as

$$\Delta E_{\text{lr}}^{\sigma,q}(z_0) = E_{\text{isolated}}^{\sigma,q}(z_0) - E_{\text{periodic}}^{\sigma,q}(z_0), \quad (2)$$

and $\bar{V}_{\text{corr}}^{\sigma,q}(z_0, z)$ is the corrected potential at z , defined as

$$\bar{V}_{\text{corr}}^{\sigma,q}(z_0, z) = \bar{V}_{\text{ab initio}}^{\sigma,q}(z) - \bar{V}_{\text{model}}^{\sigma,q}(z_0, z), \quad (3)$$

both of which depend on the standard deviation σ and the center position z_0 of the model Gaussian charge distribution, which is written as $\frac{q}{(2\pi\sigma^2)^{3/2}} e^{-(x^2+y^2+(z-z_0)^2)/2\sigma^2}$. The overline on the potentials indicates planar averages along in-plane directions. Here, $E_{\text{isolated}}^{\sigma,q}$ represents the electrostatic energy of an isolated Gaussian charge in infinite space. $E_{\text{periodic}}^{\sigma,q}$ and $V_{\text{model}}^{\sigma,q}$ respectively denote the electrostatic energy and potential caused by a Gaussian charge under PBCs. $V_{\text{ab initio}}$ is the defect-induced potential, calculated by subtracting the bulk supercell potential from that of the defective supercell. Note that PBCs include the compensating uniform background charge. z_{far} refers to the z coordinate most distant from the defect under PBCs. The average electrostatic potential $\bar{V}_{\text{model}}^{\sigma,q}$ should be set to zero to maintain consistency with *ab initio* calculations. z_0 is excluded from the variables when it is fixed in this study. E_{corr}^{σ} depends on σ , unlike in the FNV method [18], due to the spatial nonuniformity of the dielectric profile. However, this dependence is negligibly small, so we set $\sigma = 0.5 \text{ \AA}$ and, for simplicity, omit σ from the notations henceforth.

Electrostatic energies are calculated from the formula $E = \frac{1}{2} \int V(\mathbf{r})\rho(\mathbf{r})d\mathbf{r}$, where $V(\mathbf{r})$ is the electrostatic potential and $\rho(\mathbf{r})$ represents the charge density distribution. This applies under both open and periodic boundary conditions for evaluating E_{isolated}^q and E_{periodic}^q , respectively. When the spatial charge density distribution is defined, ΔE_{lr}^q is evaluated after

determining the electrostatic potentials under both boundary conditions. This is done by solving the Poisson equation [11]:

$$-\varepsilon_{0,\parallel}(z) \left(\frac{\partial^2}{\partial x^2} + \frac{\partial^2}{\partial y^2} \right) V(\mathbf{r}) - \frac{\partial}{\partial z^2} (\varepsilon_{0,\perp}(z) V(\mathbf{r})) = \rho(\mathbf{r}). \quad (4)$$

Here, $\varepsilon_{0,\parallel}$ and $\varepsilon_{0,\perp}$ represent the lateral (in-plane) and vertical (out-of-plane) dielectric profiles, respectively, at the long-wavelength limit. These profiles are sums of ion-clamped and ionic dielectric constants. Hereafter, we omit the 0 and write them as ε_{\parallel} and ε_{\perp} unless we need to explicitly distinguish the electronic and ionic components.

Noh *et al.* [14] and Komsa *et al.* [11] originally determined E_{isolated}^q by extrapolating E_{periodic}^q calculated at various supercell sizes to the infinite spacing limit. However, as emphasized in the literature [19,20], the scaling behavior of electrostatic energies in slab systems is nonmonotonic, and accurately estimating E_{isolated}^q necessitates large slab model calculations. This extrapolation can be avoided if we adopt the formula subsequently derived by Sundararaman and Ping [21] for computing E_{isolated}^q using the truncated Green's function methodology [21], which is written as

$$E_{\text{isolated}}^q = q^2 \int_0^{\infty} k e^{-k^2 \sigma^2} U_k dk, \quad (5)$$

where

$$U_k = \sum_{G',G} e^{i(G-G')z_0 - (G^2+G'^2)\sigma^2/2} D_{G'G}^{-1} \quad (6)$$

and the Hermitian

$$D_{G'G} = \delta_{G'G} \frac{L(k^2 + G^2)}{1 - e^{-kL/2} \cos(GL/2)} + L \widetilde{\Delta \varepsilon_{\perp, G'-G} G'G} + L \widetilde{\Delta \varepsilon_{\parallel, G'-G} k^2}. \quad (7)$$

Here, $G = \frac{2\pi n}{L_z}$ is the reciprocal lattice, where L_z is the side of the supercell along the z direction and n is an integer. $\widetilde{\Delta \varepsilon_{i, G}}$ ($i = \parallel, \perp$) is the Fourier transform of $\varepsilon_i(z) - 1$, and $\delta_{G'G}$ is the Kronecker's delta. The denominator of the first term in Eq. (7) appears as a consequence of the truncation of the Green's function. We can estimate E_{isolated}^q from the simple numerical integration in Eq. (5) (see also Ref. [19]).

The charge center, denoted as z_0 , generally varies depending on the specific combination of the defect and charge. For example, when hydrogen is absorbed on the oxide surface in a +1 charge state (protonic state), it forms a strong H-O bond. Conversely, in a -1 charge state (hydride state), this typically results in a longer H-O bond distance.

Note that Eq. (7) is an extension of the original formula [21] that enables the utilization of different ε_{\parallel} and ε_{\perp} . When the 2D systems exhibit in-plane anisotropy, Eqs. (5)–(7) are not applicable, and E_{isolated}^q for each defect and charge combination must be estimated through extrapolation as demonstrated in Refs. [11,14], which requires substantial computational effort. In this study, to avoid calculating ΔE_{lr}^q in Eq. (2) for all defect-charge combinations, we propose evaluating them using interpolation of ΔE_{lr}^q as a function of z_0 (see Sec. IV C).

III. CALCULATION CONDITIONS

The first-principles calculations were performed using the projector augmented-wave (PAW) method [22,23] implemented in VASP [24]. PAW data sets with radial cutoffs of 1.46, 1.01, 0.90, 0.79, and 0.58 Å for Mo, S, B, N, and H, respectively, are employed. Mo 4*p*, 5*s*, and 4*d*; S 3*s* and 3*p*; B 2*s* and 2*p*; N 2*s* and 2*p*; and H 1*s* orbitals are considered as valence electrons. We adopted the Perdew-Burke-Ernzerhof functional tuned for solids (PBEsol) [25]. For structure optimization and band structure calculations, the *k*-point sampling density was set to 2.5 Å⁻¹. The force convergence criterion was set to 5 meV/Å, while the cutoff energies were set to 336 (259) and 520 (400) eV for the calculations of SL MoS₂ and h-BN with (without) lattice constant relaxation, respectively. The relaxed in-plane lattice constants are 3.138 and 2.505 Å for SL MoS₂ and h-BN, respectively. The dielectric constants were evaluated based on the density functional perturbation theory [26,27] with doubled *k*-point density along in-plane directions.

In Sec. V, we discuss the accuracy of the corrections on the defect formation energy E_f [28,29], which is defined as

$$E_f[D^q] = \{E[D^q] + E_{\text{corr}}[D^q]\} - E_P - \sum n_i \mu_i + q(\epsilon_{\text{VBM}} + \Delta\epsilon_F), \quad (8)$$

where $E[D^q]$ and E_P are the total energies of the slab model with defect D in charge state q and the pristine model without any defect, respectively. We discuss relative defect formation energies as a function of the model size and corrections to them; thus, only $E[D^q] + E_{\text{corr}}[D^q] - E_P$ has meaning in this study.

For the point defect calculations, the in-plane lattice constants were fixed at those of the pristine models. Random displacement is helpful in identifying the most stable structure; however, it also introduces errors into the calculated formation energies due to the numerical convergence threshold in force calculations, and minimizing such errors is crucial to assess the accuracy of the corrections precisely. Therefore, in this study, the initial neighboring atoms were not displaced to increase the accuracy of E_f . The *k*-point sampling density was set to 1.8 Å⁻¹ for the defect calculations.

For the performance test, we considered a hydrogen adatom in the +1 charge state ($\text{H}_{\text{ad}}^{+1}$) on top of S in SL MoS₂ [30] and N in SL h-BN. We also considered a Mn impurity substituted on the Mo site in the +1 charge state ($\text{Mn}_{\text{Mo}}^{+1}$) and a single Mo and six S multiple-vacancy clusters in the -2 charge state ($\text{Va}_{\text{MoS}_6}^{-2}$) for SL MoS₂ [11] and C on B in the +1 charge state (C_{B}^{+1}) and H on B in the -2 charge state (H_{B}^{-2}) for SL h-BN. The in-plane supercell size was then set to 6, 9, 12, 15, and 18, while the perpendicular dimension L_z was set to 15, 20, 25, or 30 Å.

All the VASP input settings were generated using the VISE code [31] (version 0.6.6). The processing related to defects was conducted with PYDEFECT [31]. For this study, we developed the PYDEFECT_2D code [32]. This code automates the

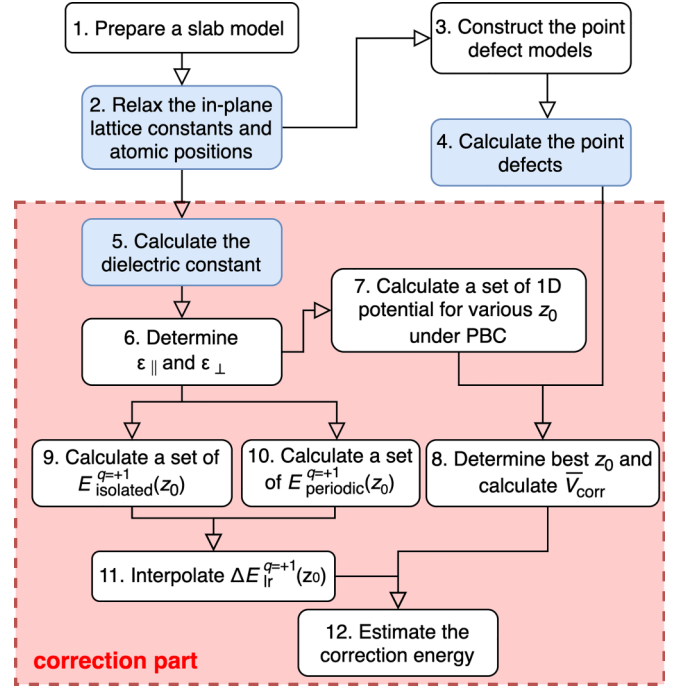


FIG. 1. Workflow to estimate the corrections to the point defect formation energies in 2D materials. The steps involving first-principles calculations are colored blue. Steps 6–12 are done with PYDEFECT_2D.

energy corrections of defects in 2D materials. It can be used in conjunction with PYDEFECT.

IV. DETAILS OF THE CORRECTION WORKFLOW

The NK correction technique is based on the concept that the defect charge is contained within the supercell, which is a typical prerequisite in corrections to charged defects. It is also necessary to define the functional form of the dielectric profile. Our goal is to evaluate the corrections of E_f using Eqs. (1)–(3). The workflow is depicted in Fig. 1. Since the steps 1–4 are common in conventional point defect calculations, we begin with step 5.

A. Dielectric profiles (steps 5 and 6)

The dielectric profile is divided into the ion-clamped part ϵ_∞ , which is a sum of electronic and vacuum permittivity, and the ionic part ϵ_{ion} . The value of ϵ_∞ along the z direction ($\epsilon_{\infty, \perp}$) is assessed by introducing a dipole layer into a vacuum and calculating the gradient of the electrostatic potential. However, determining ϵ_∞ in the in-plane direction is challenging using the same method due to the absence of a vacuum region laterally. Inserting a dipole layer within materials introduce artifacts in the electronic structure calculation. Moreover, calculating ϵ_{ion} is difficult since the defect-induced electrostatic potential is not smooth anymore after the atomic positions are relaxed. Hence, there is a need for defining the dielectric profiles.

In the literature, two functional forms are commonly utilized [7,11]: the stepwise function with smoothed edges,

TABLE I. Ion-clamped (ϵ_∞) and ionic (ϵ_{ion}) dielectric constants along the lateral (\parallel) and vertical (\perp) directions that are calculated using the slab models with $L_z = 20 \text{ \AA}$.

	$\epsilon_{\infty, \parallel}^{\text{ave}}$	$\epsilon_{\infty, \perp}^{\text{ave}}$	$\epsilon_{\text{ion}, \parallel}^{\text{ave}}$	$\epsilon_{\text{ion}, \perp}^{\text{ave}}$	$\epsilon_{0, \parallel}^{\text{ave}}$	$\epsilon_{0, \perp}^{\text{ave}}$
SL MoS ₂	5.19	1.34	0.07	0.00	5.26	1.34
SL h-BN	1.64	1.12	0.29	0.01	1.93	1.12

defined as

$$\epsilon(z) = 1 + A \left[1 + \text{erf}\left(\frac{z - z_{\text{left}}}{\beta}\right) \right] \left[1 + \text{erf}\left(\frac{z_{\text{right}} - z}{\beta}\right) \right], \quad (9)$$

where A represents the scaling parameter, z_{left} and z_{right} are the boundaries of the slab layer on the left and right sides, respectively, and β is the parameter for edge smearing, and the Gaussian-type function, expressed as

$$\epsilon(z) = 1 + B \exp\left(-\frac{(z - z_0)^2}{2\sigma_\epsilon^2}\right), \quad (10)$$

where B is the scaling parameter, z_0 is the Gaussian function's center, and σ_ϵ is the Gaussian smearing parameter. The latter is frequently applied to atomically thin 2D systems, where all atoms are coplanar, as observed in h-BN. Considering the displacement of the S and Mo planes in the z direction, we adopt the stepwise profile for SL MoS₂.

The method for determining dielectric profiles varies significantly in the literature [7,8,10–14]. However, the dielectric profiles should at least be consistent with the average dielectric constants calculated using the same *slab model* ϵ^{ave} [11]. Note that the relationship between ϵ^{ave} and the dielectric profile is dependent on the direction: $\epsilon_{\parallel}^{\text{ave}}$ and $\epsilon_{\perp}^{\text{ave}}$ correspond to those of capacitors connected in *parallel* and in *series*, respectively, and can be expressed as

$$\epsilon_{\parallel}^{\text{ave}} = \frac{1}{L_z} \int_0^{L_z} \epsilon_{\parallel}(z) dz \quad (11)$$

and

$$(\epsilon_{\perp}^{\text{ave}})^{-1} = \frac{1}{L_z} \int_0^{L_z} \epsilon_{\perp}^{-1}(z) dz. \quad (12)$$

The scaling parameters A and B are determined to satisfy these formula.

As examples, Table I shows ϵ^{ave} of SL MoS₂ and SL h-BN at $L_z = 20 \text{ \AA}$. Interestingly, $\epsilon_{\parallel}^{\text{ave}}$ (5.26) and $\epsilon_{\perp}^{\text{ave}}$ (1.34) differ significantly in SL MoS₂. However, this difference is not primarily due to variations in the dielectric constants within the 2D materials. Rather, it arises from the differences between the averaging formulas in Eqs. (11) and (12).

Figures 2(a) and 2(b) display the lateral and vertical dielectric profiles of SL MoS₂ and SL h-BN, respectively, for different step function widths w and Gaussian smearing parameters σ_ϵ , derived from the same ϵ^{ave} as in Table I. The intermediate width of SL MoS₂ ($w = 5.15 \text{ \AA}$) is determined from the boundaries where the average charge density becomes $1.0 |e|/\text{\AA}^2$, while that of SL h-BN ($\sigma_\epsilon = 0.783 \text{ \AA}$) is taken from Ref. [11], where it is also determined from the charge density. Figures 2(c) and 2(d) illustrate the heights

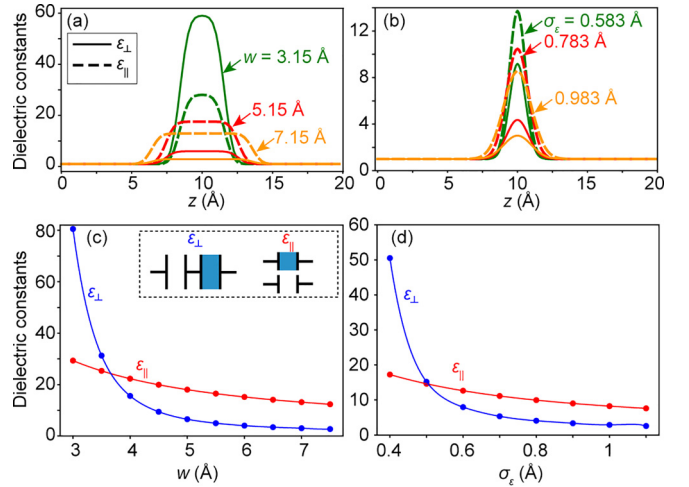


FIG. 2. (a) Dielectric profiles of SL MoS₂ at three different step function widths w , 3.15, 5.15, and 7.15 \AA . The edge smearing parameter is set to 0.5 \AA . (b) Those of SL h-BN at three different Gaussian widths σ_ϵ , 0.583, 0.783, and 0.983 \AA . Dielectric constants at the centers of the (c) SL MoS₂ and (d) SL h-BN slabs as a function of w and σ_ϵ , respectively. The inset in (c) shows the schematics of the equivalent circuits for calculating averaged dielectric constants along the perpendicular (\perp ; left) and parallel (\parallel ; right) directions.

of ϵ_{\parallel} and ϵ_{\perp} at the centers of the slabs as w and σ_ϵ vary, respectively. It is evident that the height of ϵ_{\perp} decreases more steeply than ϵ_{\parallel} with increasing w and σ_ϵ . The dielectric profiles largely depend on the choice of parameters, but this does not significantly affect the correction energies when defects exist in the slabs. However, when defects are located far from the surfaces, such as adsorbed ions, the dielectric profiles are likely related to relatively large errors, as will be shown later (see Sec. V A).

B. z_0 and V_{corr} (steps 7 and 8)

The next steps involve the determination of the model Gaussian charge position z_0 . One may expect that z_0 corresponds to a defect site, e.g., a vacant site or an impurity site itself. We demonstrate \bar{V}_{corr} of $\text{H}_{\text{ad}}^{+1}$ on the SL MoS₂ calculated by setting z_0 to the proton site in Fig. 3(a). There is an obvious gradient of $\bar{V}_{\text{corr}}(z)$ (\bar{V}'_{corr}) in a vacuum, indicating the presence of the macroscopic dipole. Therefore, the proton site is not adequate as z_0 , and its fine tuning is necessary for evaluating E_{corr} , as discussed in Ref. [8].

To automatically determine the optimized z_0 (z_0^{opt}) that fully eliminate the macroscopic dipole, we propose the following workflow:

(1) Calculate $\bar{V}_{\text{model}}(z_0, z)$ for different z_0 under 1D PBCs. Due to the dimensionality reduction, the computational cost is negligibly small. The potentials are reusable for any defect charge combination.

(2) Compute $\bar{V}_{\text{ab initio}}(z)$ from first-principles calculations.

(3) For different z_0 considered in step 1, compute $\bar{V}_{\text{corr}}(z_0, z) = \bar{V}_{\text{ab initio}}(z) - \bar{V}_{\text{model}}(z_0, z)$ and estimate its derivative, i.e., electric field \bar{V}'_{corr} at z_{far} [$\bar{V}'_{\text{corr}}(z_0, z_{\text{far}})$].

(4) Select z_0 with the smallest absolute value of $\bar{V}'_{\text{corr}}(z_0, z_{\text{far}})$ as z_0^{opt} .

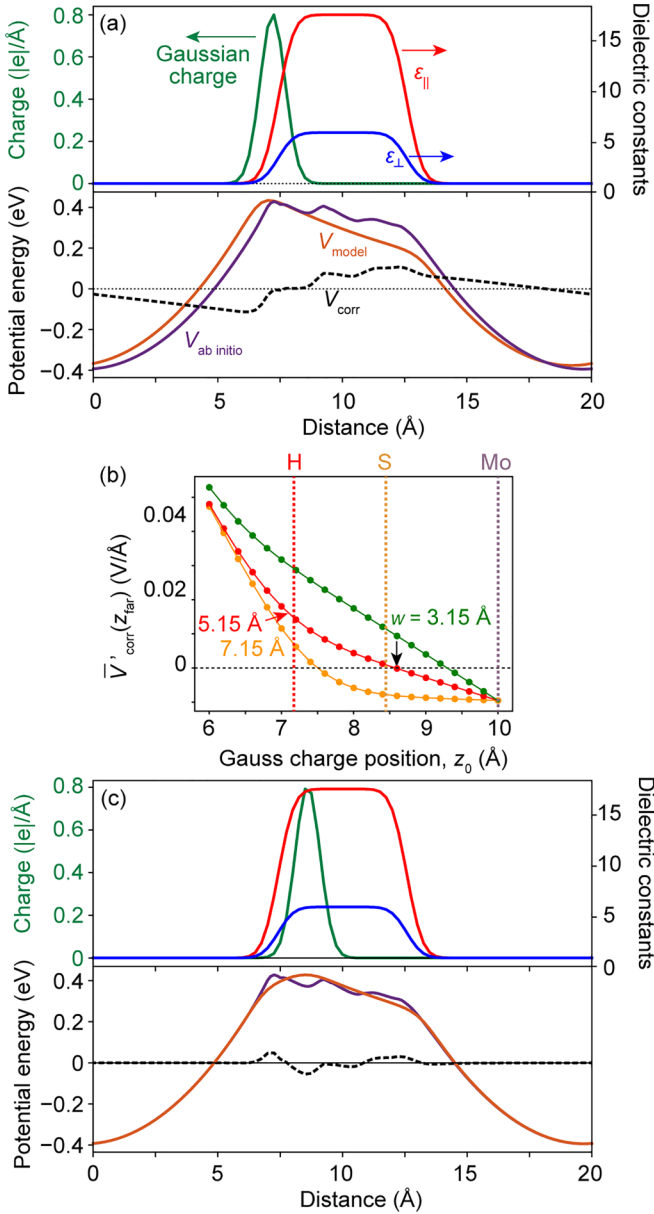


FIG. 3. (a) Dielectric profiles and planar-averaged Gaussian charge distribution (top) and $\bar{V}_{ab\text{ initio}}$, \bar{V}_{model} , and \bar{V}_{corr} of the $\text{H}_{\text{ad}}^{+1}$ model on SL MoS₂ with 6×6 in-plane size and $L_z = 20 \text{ \AA}$ (bottom; see text for details). The charge center z_0 is set to the protonic position. (b) Electric field at the point farthest from the Gaussian charge in the z direction $\bar{V}'_{\text{corr}}(z_{\text{far}})$ as a function of the Gauss charge position z_0 . Results calculated with the three different dielectric (z_0) profiles in Fig. 2(a) are shown. The vertical dashed lines indicate the atomic positions of Mo, S, and absorbed H, while the black arrow indicates z_0^{opt} . (c) Same as (a), but for $z_0 = z_0^{\text{opt}}$ in this study (see text for details).

Figure 3(b) displays the variation of $\bar{V}'_{\text{corr}}(z_{\text{far}})$ for $\text{H}_{\text{ad}}^{+1}$ as a function of z_0 , utilizing the three distinct dielectric profiles illustrated in Fig. 2(a). Crucially, the optimal value of z_0^{opt} varies depending on the dielectric profile, yet for all profiles, z_0^{opt} shifts from the proton towards the SL MoS₂, indicating electron transfer from SL MoS₂ to $\text{H}_{\text{ad}}^{+1}$. Figure 3(c) presents

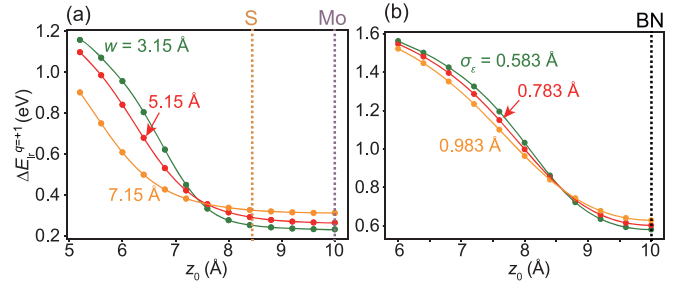


FIG. 4. The long-range correction energy $\Delta E_{\text{lr}}^{q=+1}$ of a Gaussian charge in the slab models with a 6×6 in-plane size and $L_z = 20 \text{ \AA}$. The three different dielectric profiles in Figs. 2(a) and 2(b) are considered.

$\bar{V}_{\text{corr}}(z_0^{\text{opt}}, z)$, where a flat potential is observed in vacuum, underscoring the efficacy of this workflow.

C. $\Delta E_{\text{lr}}^q(z_0)$ (steps 9–11)

Generally speaking, $\Delta E_{\text{lr}}^q(z_0^{\text{opt}})$ is required for individual defect charge combinations. As discussed above, many calculations of ΔE_{lr}^q should be avoided due to their high computational costs. In this study, we propose estimating ΔE_{lr}^q by interpolation. Figures 4(a) and 4(b) show $\Delta E_{\text{lr}}^{q=+1}$ for SL MoS₂ and SL h-BN, respectively, as a function of z_0 for the three dielectric profiles shown in Fig. 2(a). When the dielectric profile is smooth, $\Delta E_{\text{lr}}^{q=+1}(z_0)$ is effectively fitted as shown in Fig. 4. Once the interpolated function is obtained, we can evaluate ΔE_{lr}^q from $\Delta E_{\text{lr}}^q = q^2 \Delta E_{\text{lr}}^{q=+1}$. This interpolation is extremely useful for low-symmetry materials because they require very high computational costs for evaluating ΔE_{lr}^q , as mentioned above.

V. RESULTS AND DISCUSSION

A. Dependence of E_{corr} on dielectric profiles

As mentioned earlier, the functional form of the dielectric profile is an input parameter. Given the inherent uncertainty in the dielectric profile, it is crucial to understand the sensitivity of formation energies for meaningful discussions in practical applications. E_{corr} is obtained by summing $\Delta E_{\text{lr}}^q(z_0^{\text{opt}})$ obtained in step 11 and $q\bar{V}_{\text{corr}}(z_0^{\text{opt}}, z_{\text{far}})$ obtained in step 8 in Fig. 1. $q\bar{V}_{\text{corr}}(z_0^{\text{opt}}, z_{\text{far}})$ is inversely proportional to the supercell volume and is usually negligibly small because the defect models for 2D materials typically have a large vacuum. Thus, ΔE_{lr}^q closely represents E_{corr} .

As shown in Fig. 4(a), $\Delta E_{\text{lr}}^{q=+1}$ within the SL MoS₂ slab are relatively insensitive to the dielectric profile, consistent with Ref. [11]. However, variations increase when moving from the middle of the slab towards the vacuum. These variations are attributed to errors caused by the selection of an ill-defined dielectric profile. Therefore, it is important to keep in mind that defects with charge centers distanced from the surfaces may exhibit significant errors. In the case of SL h-BN, as illustrated in Fig. 4(b), these variations are more reduced, primarily due to the smaller dielectric constant within the slab and the reduced thickness of the single layer.

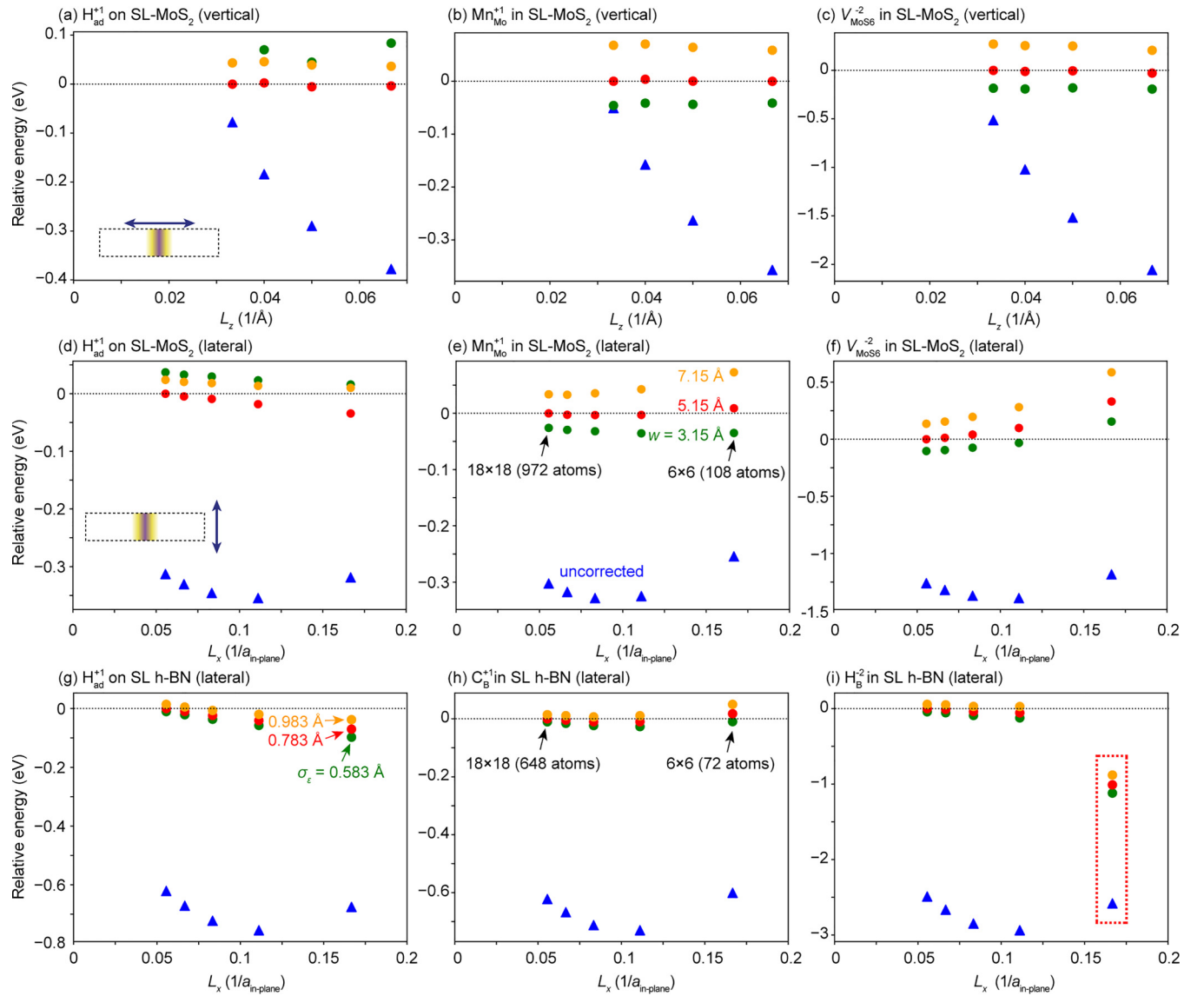


FIG. 5. Cell size dependences of defect formation energies E_f of (a) and (d) H_{ad}^+ on SL-MoS₂, (b) and (e) Mn_{Mo}^+ , (c) and (f) $V_{\text{MoS}_6}^{-2}$ in SL MoS₂, (g) H_{ad}^+ on SL h-BN, (h) C_{B}^+ , and (i) H_{B}^2 in SL h-BN with and without corrections. (a)–(c) show the results as a function of the inverse of the vertical distance of the supercells L_z , with a fixed in-plane size of 6×6 . (d)–(i) show the results as a function of the inverse of the horizontal in-plane size L_x , with $L_z = 20 \text{ \AA}$. The units in (d)–(i) are the inverse of the in-plane lattice constants $a_{\text{in-plane}}$. The energy zeros are set to the energies obtained for the largest supercells corrected with the dielectric profiles with intermediate widths. The three different dielectric profiles shown in Figs. 2(a) and 2(b) are considered for each. The result in (i) highlighted by the red rectangle exhibits an unintended electron trap in a vacuum (see text for details).

Figures 5(a)–5(c) and 5(d)–5(i) illustrate E_f with and without corrections as a function of L_z and in-plane dimension L_x , respectively. Although the model size dependences have been examined in terms of L_z [7,8,11], this study also investigates dependences on L_x . Note that when either L_x or L_z is extended while the other is kept fixed, the uncorrected E_f diverges towards positive infinity. This divergence is mitigated upon applying the corrections in all cases, resulting in E_f remaining nearly constant as L_z or L_x is increased. However, this does not necessarily indicate the accuracy of the corrections, as the corrected E_f in Fig. 5 do not converge to identical values across different dielectric profiles. This discrepancy is attributed to spurious interactions along the fixed direction. To accurately determine E_f in the dilution limit, isotropic

expansion of supercells is required, but it is computationally prohibitive.

We observe a significant energy lowering of E_f in Fig. 5(i) when the in-plane lattice constant is expanded to 6×6 . This discrepancy arises from an unintended electron trap in the central portion of the vacuum region, resulting from a background charge (see also Ref. [7]). Because the background charge density is inversely proportional to the volume, this artifact is absent in the calculations of the 9×9 supercell or larger.

Regarding defects in SL MoS₂ [Figs. 5(a)–5(f)], the corrected E_f does not depend on L_z , while a slight cell size dependence is observed when changing L_x . As mentioned by Freysoldt and Neugebauer [8], the electrostatic interactions in the vertical directions are irrelevant to the details of the

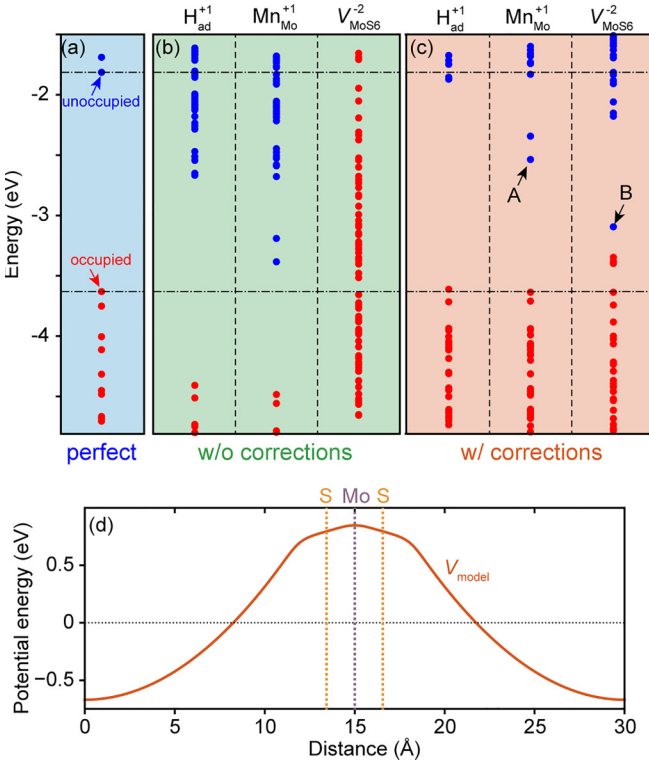


FIG. 6. (a) Eigenvalues of perfect SL MoS₂ and (b) those of the 6×6 supercell including H_{ad}⁺, Mn_{Mo}⁺, and Va_{MoS6}⁻² defects. L_z is set to 30 Å. (c) The eigenvalues corrected by subtracting the potential for electrons at $z = 15$ Å (Mo layer) as shown in (d). The spatial distributions of the eigenstates denoted as A and B are shown in Figs. 7(a) and 7(b), respectively. Red and blue dots indicate the occupied and unoccupied states, respectively. (d) The planar averaged potential profile of the Gaussian model \bar{V}_{model} with $z_0 = 15$ Å in the 6×6 supercell. The dielectric profile with $w = 5.15$ Å shown in Fig. 2(a) is adopted. The Mo and S positions are indicated by dashed lines.

dielectric profile when Eq. (12) is satisfied. However, the interactions in the lateral directions are inversely proportional to the dielectric constants, which introduces the in-plane size dependence [Figs. 5(d)–5(f)]. Compared to defects in SL MoS₂, those in SL h-BN exhibit smaller dependences on the dielectric profile. The reason is attributed to the smaller dependence of $E_{\text{fr}}^{q=+1}$ (Fig. 4) as mentioned earlier.

Defects with larger $|q|$ may have greater potential errors because E_{fr}^q is proportional to q^2 . This is particularly pronounced for defects situated far from the surface of SL MoS₂ owing to the more significant dielectric profile dependence. Indeed, the cell size dependence of E_f with corrections for Va_{MoS6}⁻² in SL MoS₂ is relatively large, as demonstrated in Fig. 5(f).

B. Corrections on eigenvalues of host bands

In the point defect calculations, analyzing electronic eigenvalues is crucial for identifying the presence and energy positions of perturbed host states and defect localized states [33–35]. In Figs. 6(a) and 6(b), the eigenvalues of pristine SL MoS₂ where the in-plane lattice constant is expanded to

6×6 and those in supercells including H_{ad}⁺, Mn_{Mo}⁺, and Va_{MoS6}⁻² are shown, respectively. It is evident that in the presence of the positively (negatively) charged defects, the eigenvalues are significantly downward (upward) shifted from those in the pristine slab model. Such shifts are introduced by an electric field caused by the defect and background charge. As exemplified in Fig. 3(c), in regions where SL MoS₂ exists, the positive (negative) potential operates if the defect charge is positive (negative). Because the host bands in 2D materials are distributed within the MoS₂ plane, we need to subtract the electrostatic potential on the MoS₂ plane from the eigenvalues.

Figure 6(d) illustrates \bar{V}_{model} in the model where a Gaussian charge is placed at the center of the SL MoS₂. Note that the potential for electrons is the negative of \bar{V}_{model} , so the corrections are achieved by adding $\bar{V}_{\text{model}}(z = 15\text{Å})$. Figure 6(c) displays the constantly shifted eigenvalues of the supercells with defects. The eigenvalues corresponding to the host bands are accurately reproduced in all three calculations, and the defect levels are distinctly discerned. Note that the precision of the corrections to the host-derived eigenvalues is not quantified by comparing those in the pristine supercell. This is because the host-derived orbitals are altered by the point defects, and some deviation of eigenvalues from those in the pristine 2D materials may inherently occur.

In 3D materials, the host-derived bands distribute across the entire cell, and the average potential remains approximately zero, even if a background charge is present. Therefore, such corrections are necessary only for defects in lower-dimensional models including a vacuum.

C. Corrections to eigenvalues of defect states

The defect localized states necessitate different corrections from the host-derived bands, which can be estimated using the relation proposed by Chen and Pasquarello [36], known as

$$\epsilon_{\text{corr}} = -\frac{2}{q}E_{\text{corr}}. \quad (13)$$

The corrected eigenvalues are comparable with the band edges in the corresponding pristine slab model. However, in slab calculations, the potential reference depends on the vacuum region in low-dimensional models because the average electrostatic potential is set to zero. Therefore, to discuss the eigenvalues between supercells with different L_z , they must be aligned with the vacuum level.

Figures 7(a) and 7(b) depict the spatial distributions of squared wave functions for two defect levels in Mn_{Mo}⁺ and Va_{MoS6}⁻², labeled A and B in Fig. 6(c), respectively. Both levels exhibit strong localization. Figures 7(c) and 7(d) display the eigenvalues relative to the vacuum level as a function of L_z . Without corrections, eigenvalues monotonically decrease (increase) for positively (negatively) charged defects with increasing L_z . Conversely, corrected eigenvalues using Eq. (13) remain nearly constant, affirming their validity. Nevertheless, these corrected eigenvalues can vary by several tens of eV, depending on the dielectric profile selection. Thus, a careful choice of dielectric profile, considering factors such as charge density distribution, is crucial for accurate corrections.

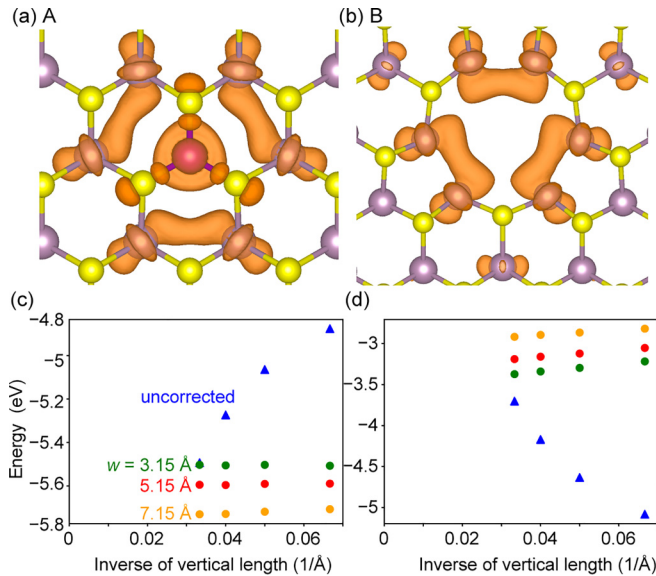


FIG. 7. (a) and (b) Squared wave functions denoted as A and B in Fig. 6(c). Visualization is performed with VESTA [37]. (c) and (d) The eigenvalues with and without corrections with respect to the vacuum level as a function of the inverse of L_z . For the corrections, the three dielectric profiles shown in Fig. 2 are considered. The in-plane size is fixed to the 6×6 supercell.

Furthermore, it is vital to interpret calculation results within the variation.

VI. CONCLUSIONS

In this study, the PYDEFECT_2D code was developed to automate corrections to point defect formation energies and eigenvalues in 2D materials. Our method builds on the approach proposed by Noh *et al.* [14] and Komsa *et al.* [11] and utilizes the self-energy computation of isolated Gaussian charges based on the formalism by Sundararaman and Ping [21]. To reduce computational costs and processing time, interpolation of the long-range electrostatic interaction was proposed along with estimation of the potential alignment term from 1D potentials. Unfortunately, the dielectric profiles employed in these corrections are ill defined. Thus, we examined how the choice of dielectric profiles affects the correction energies and eigenvalues. Through the test calculations of three different types of defects in MoS₂ and h-BN, it was found that the selection of dielectric profiles can relatively influence the corrections for adsorbed atoms. To address the artificial shifts of host-derived eigenvalues, aligning the potential in the region where the 2D material is present was suggested. The precision of our corrections and previously proposed defect-induced eigenvalue corrections were also evaluated. We believe that our developed code, computational techniques, and extensive tests contribute significantly to the study of point defects in 2D materials.

ACKNOWLEDGMENTS

Discussions with S. Bae are sincerely appreciated. I also appreciate the advice from Prof. R. Sundararaman for the

implementation of the self-energy computation of isolated Gaussian charges. This study was financially supported by KAKENHI (Grant No. 22H01755) and the E-IMR project at IMR, Tohoku University.

APPENDIX: SUMMARY OF THE CORRECTION METHODS

Other than the NK method, various types of correction techniques for defects in 2D models have been proposed [7–17]. For example, da Silva *et al.* proposed a method to correct the electrostatic potential in self-consistent field calculations to reproduce the potential under open boundary conditions [7]. This method prevents artificial strong electric fields in the vacuum and accurately reproduces the electronic structure in the dilute limit. However, this technique does not allow for the relaxation of atomic positions, which may result in significant errors in the formation energies of charged defects in ionic compounds. Freysoldt and Neugebauer (FN) proposed an *a posteriori* technique to evaluate the correction energy using the image charge method [8] which is nearly as accurate as the NK method. The method proposed by Vinichenko *et al.* [12] is similar to the NK method, but it suggests calculating the long-range correction energy using the defect charge density. However, this approach may be challenging to apply if the defect charge state is submerged in the valence or conduction bands.

Note that most of these correction methods necessitate knowledge of the dielectric profiles. An exception is the method proposed by Wang *et al.* [15], in which the supercell model is scaled to eliminate spurious electrostatic interaction. While this method obviates the need for postcorrections, it does not accommodate the site dependence of the correction energies. A similar method is the special vacuum (SV) method proposed by Komsa *et al.* [11], in which the supercell model is determined in a like manner. The difference lies in the fact that, in Wang’s method, the scaling is established by a series of first-principles calculations on various slab sizes, whereas in the SV method, it is deduced from Gaussian charge models under an assumed dielectric profile.

The advantages and disadvantages of the correction methods are summarized from three perspectives as follows and in Table II.

(1) *Ionic relaxation.* da Silva *et al.*’s method does not support the relaxation of ionic positions, a critical aspect for ionic compounds. Conversely, other methods can account for relaxation effects by employing a dielectric profile that includes both electronic and ionic contributions (in the NK,

TABLE II. Summary of the differences between correction methods for charged point defects in 2D materials. An asterisk indicates a situation where an isotropic dielectric profile is assumed.

	NK	FN	da Silva	Wang	SV
Allow ionic relaxation	✓	✓	✗	✓	✓
Require dielectric profile	✓	✓*	✓*	✗	✓
Require defect center	✓	✓	✓	✗	✗

FN, and SV methods) or by conducting scaling calculations that incorporate ionic relaxation (in Wang's method).

(2) *Dielectric profile.* da Silva *et al.*'s method and the FN method currently assume a three-dimensionally isotropic dielectric profile, which may be unsuitable for materials exhibiting distinct screening behaviors in lateral versus vertical directions. While the NK and SV methods suit lower-dimensional systems, they face limitations when in-plane dielectric profiles are anisotropic. In such cases, extrapolating E_{periodic} becomes necessary to calculate E_{isolated}^q . Although

Wang's method circumvents the need for a dielectric profile, it demands multiple defect calculations across varying supercell sizes, leading to substantial computational expense.

(3) *Defect center.* The methods developed by Komsa *et al.*, FN, and da Silva *et al.* necessitate specifying the defect center's position, whereas Wang's method and the SV method do not. However, the latter methods cannot account for the dependence of the correction energy on the defect center, which may lead to significant errors for absorbed ions.

-
- [1] F. Schwierz, J. Pezoldt, and R. Granzner, Two-dimensional materials and their prospects in transistor electronics, *Nanoscale* **7**, 8261 (2015).
- [2] D. Deng, K. S. Novoselov, Q. Fu, N. Zheng, Z. Tian, and X. Bao, Catalysis with two-dimensional materials and their heterostructures, *Nat. Nanotechnol.* **11**, 218 (2016).
- [3] J. Wang, V. Malgras, Y. Sugahara, and Y. Yamauchi, Electrochemical energy storage performance of 2D nanoarchitected hybrid materials, *Nat. Commun.* **12**, 3563 (2021).
- [4] D. Tyagi, H. Wang, W. Huang, L. Hu, Y. Tang, Z. Guo, Z. Ouyang, and H. Zhang, Recent advances in two-dimensional-material-based sensing technology toward health and environmental monitoring applications, *Nanoscale* **12**, 3535 (2020).
- [5] M. C. Lemme, D. Akinwande, C. Huyghebaert, and C. Stampfer, 2D materials for future heterogeneous electronics, *Nat. Commun.* **13**, 1392 (2022).
- [6] S. M. Hus and A.-P. Li, Spatially-resolved studies on the role of defects and boundaries in electronic behavior of 2D materials, *Prog. Surf. Sci.* **92**, 176 (2017).
- [7] M. Chagas da Silva, M. Lorke, B. Aradi, M. Farzalipour Tabriz, T. Frauenheim, A. Rubio, D. Rocca, and P. Deák, Self-consistent potential correction for charged periodic systems, *Phys. Rev. Lett.* **126**, 076401 (2021).
- [8] C. Freysoldt and J. Neugebauer, First-principles calculations for charged defects at surfaces, interfaces, and two-dimensional materials in the presence of electric fields, *Phys. Rev. B* **97**, 205425 (2018).
- [9] C. Freysoldt, A. Mishra, M. Ashton, and J. Neugebauer, Generalized dipole correction for charged surfaces in the repeated-slab approach, *Phys. Rev. B* **102**, 045403 (2020).
- [10] D. Wang and R. Sundararaman, Layer dependence of defect charge transition levels in two-dimensional materials, *Phys. Rev. B* **101**, 054103 (2020).
- [11] H.-P. Komsa, N. Berseneva, A. V. Krasheninnikov, and R. M. Nieminen, Charged point defects in the flatland: Accurate formation energy calculations in two-dimensional materials, *Phys. Rev. X* **4**, 031044 (2014).
- [12] D. Vinichenko, M. G. Sensoy, C. M. Friend, and E. Kaxiras, Accurate formation energies of charged defects in solids: A systematic approach, *Phys. Rev. B* **95**, 235310 (2017).
- [13] M. H. Naik and M. Jain, Coffee: Corrections for formation energy and eigenvalues for charged defect simulations, *Comput. Phys. Commun.* **226**, 114 (2018).
- [14] J.-Y. Noh, H. Kim, and Y.-S. Kim, Stability and electronic structures of native defects in single-layer MoS₂, *Phys. Rev. B* **89**, 205417 (2014).
- [15] D. Wang, D. Han, X.-B. Li, S.-Y. Xie, N.-K. Chen, W. Q. Tian, D. West, H.-B. Sun, and S. B. Zhang, Determination of formation and ionization energies of charged defects in two-dimensional materials, *Phys. Rev. Lett.* **114**, 196801 (2015).
- [16] F. Wu, T. J. Smart, J. Xu, and Y. Ping, Carrier recombination mechanism at defects in wide band gap two-dimensional materials from first principles, *Phys. Rev. B* **100**, 081407(R) (2019).
- [17] T. J. Smart, F. Wu, M. Govoni, and Y. Ping, Fundamental principles for calculating charged defect ionization energies in ultrathin two-dimensional materials, *Phys. Rev. Mater.* **2**, 124002 (2018).
- [18] C. Freysoldt, J. Neugebauer, and C. Van de Walle, Fully *ab initio* finite-size corrections for charged-defect supercell calculations, *Phys. Rev. Lett.* **102**, 016402 (2009).
- [19] H.-P. Komsa, N. Berseneva, A. V. Krasheninnikov, and R. M. Nieminen, Erratum: Charged point defects in the flatland: Accurate formation energy calculations in two-dimensional materials [Phys. Rev. X **4**, 031044 (2014)], *Phys. Rev. X* **8**, 039902(E) (2018).
- [20] C. Freysoldt, J. Neugebauer, A. M. Z. Tan, and R. G. Hennig, Limitations of empirical supercell extrapolation for calculations of point defects in bulk, at surfaces, and in two-dimensional materials, *Phys. Rev. B* **105**, 014103 (2022).
- [21] R. Sundararaman and Y. Ping, First-principles electrostatic potentials for reliable alignment at interfaces and defects, *J. Chem. Phys.* **146**, 104109 (2017).
- [22] P. E. Blöchl, Projector augmented-wave method, *Phys. Rev. B* **50**, 17953 (1994).
- [23] G. Kresse and D. Joubert, From ultrasoft pseudopotentials to the projector augmented-wave method, *Phys. Rev. B* **59**, 1758 (1999).
- [24] G. Kresse and J. Furthmüller, Efficient iterative schemes for *ab initio* total-energy calculations using a plane-wave basis set, *Phys. Rev. B* **54**, 11169 (1996).
- [25] J. P. Perdew, A. Ruzsinszky, G. I. Csonka, O. A. Vydrov, G. E. Scuseria, L. A. Constantin, X. Zhou, and K. Burke, Restoring the density-gradient expansion for exchange in solids and surfaces, *Phys. Rev. Lett.* **100**, 136406 (2008).
- [26] S. Baroni and R. Resta, *Ab initio* calculation of the macroscopic dielectric constant in silicon, *Phys. Rev. B* **33**, 7017 (1986).
- [27] X. Gonze and C. Lee, Dynamical matrices, Born effective charges, dielectric permittivity tensors, and interatomic force constants from density-functional perturbation theory, *Phys. Rev. B* **55**, 10355 (1997).

- [28] Y. Kumagai and F. Oba, Electrostatics-based finite-size corrections for first-principles point defect calculations, *Phys. Rev. B* **89**, 195205 (2014).
- [29] F. Oba and Y. Kumagai, Design and exploration of semiconductors from first principles: A review of recent advances, *Appl. Phys. Express* **11**, 060101 (2018).
- [30] A. Singh and A. K. Singh, Origin of n -type conductivity of monolayer MoS₂, *Phys. Rev. B* **99**, 121201 (2019).
- [31] Y. Kumagai, N. Tsunoda, A. Takahashi, and F. Oba, Insights into oxygen vacancies from high-throughput first-principles calculations, *Phys. Rev. Mater.* **5**, 123803 (2021).
- [32] Y. Kumagai, PYDEFECT_2D, https://github.com/kumagai-group/pydefect_2d.
- [33] Y. Kumagai, S. R. Kavanagh, I. Suzuki, T. Omata, A. Walsh, D. O. Scanlon, and H. Morito, Alkali mono-pnictides: A new class of photovoltaic materials by element mutation, *PRX Energy* **2**, 043002 (2023).
- [34] Y. Kumagai, M. Choi, Y. Nose, and F. Oba, First-principles study of point defects in chalcopyrite ZnSnP₂, *Phys. Rev. B* **90**, 125202 (2014).
- [35] N. Tsunoda, Y. Kumagai, A. Takahashi, and F. Oba, Electrically benign defect behavior in zinc tin nitride revealed from first principles, *Phys. Rev. Appl.* **10**, 011001(R) (2018).
- [36] W. Chen and A. Pasquarello, Correspondence of defect energy levels in hybrid density functional theory and many-body perturbation theory, *Phys. Rev. B* **88**, 115104 (2013).
- [37] K. Momma and F. Izumi, VESTA a three-dimensional visualization system for electronic and structural analysis, *J. Appl. Cryst.* **41**, 653 (2008).